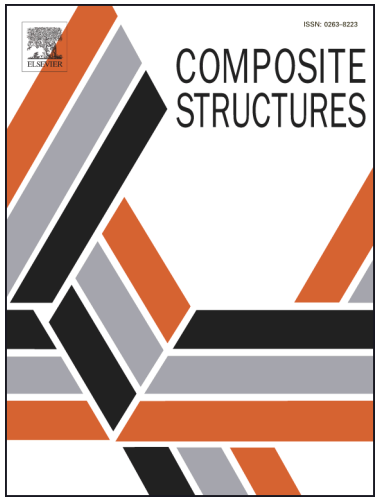

The effect of off-axis angles on the mesoscale deformation response and failure behavior of an orthotropic textile carbon-epoxy composite

Jishen Yang, Xiaoguang Yang, Hanxing Zhu, Duoqi Shi, Xindong Chen, Hongyu Qi

PII: S0263-8223(18)31059-6
DOI: https://doi.org/10.1016/j.compstruct.2018.08.010
Reference: COST 10060

To appear in: *Composite Structures*

Received Date: 19 March 2018
Revised Date: 13 July 2018
Accepted Date: 4 August 2018

Please cite this article as: Yang, J., Yang, X., Zhu, H., Shi, D., Chen, X., Qi, H., The effect of off-axis angles on the mesoscale deformation response and failure behavior of an orthotropic textile carbon-epoxy composite, *Composite Structures* (2018), doi: https://doi.org/10.1016/j.compstruct.2018.08.010

The effect of off-axis angles on the mesoscale deformation response and failure behavior of an orthotropic textile carbon-epoxy composite

Jishen Yang [a], Xiaoguang Yang [a,c,d], Hanxing Zhu [b], Duoqi Shi [a,c], Xindong Chen [b], Hongyu Qi [a,c*]

[a] *School of Energy and Power Engineering, Beihang University, Beijing, 100191, China*

[b] *School of Engineering, Cardiff University, Cardiff, CF24 3AA, UK*

[c] *Collaborative Innovation Center for Advanced Aero-Engine, Beijing 100191, China*

[d] *Nanchang Hangkong University, Nanchang, 330063, China*

Corresponding author. Tel: +86 010 82316362; fax: +86 010 82316362;

E-mail address: qhy@buaa.edu.cn (H. Qi[*])

Abstract:

The deformation response and failure behavior of an orthotropic textile carbon-epoxy composite were investigated under off-axis tensile loading. Digital image correlation (DIC) was utilized to effectively capture the full-field and mesoscale strain distribution. The macroscale mechanical performance was strongly sensitive to the fiber bundles orientation relative to the loading direction. Based on the experimental data, a quantitative relation between the rotation angle and off-axis angle was established, and a negative correlation between the failure strength and the rotation angle was observed. The underlying failure mechanisms of the specimens with different off-axis orientations were analyzed using scanning electron microscopy (SEM) and DIC techniques. The load-bearing mechanisms were different between the on- and off-axis cases. High local shear strain eventually resulted in the brushy shear-type fracture in the off-axis case, and the local micro cracks developed during the loading caused the reduction and imbalance of local load-bearing capacity.

Keywords: Textile composites; Off-axis tension; Digital image correlation(DIC); Deformation response; Failure strength; Fracture morphology.

1. Introduction

Fiber-reinforced textile composites are increasingly employed for structural components in aircraft/aerospace, automotive, civil engineering and marine industries in recent years. These materials have many advantages, e.g., outstanding mechanical and thermal properties, good chemical resistance, relatively lightweight, dimensional stability, excellent durability, and design flexibility [1–3]. Owing to the variability of textile composites, the deformation and failure response are influenced by many factors, such as the reinforcement architecture, the mechanical properties of their constituents and the interaction between the reinforcing fibers and the matrix [4,5]. So far, numerous numerical [6–10] and experimental [5,10–12] studies have been performed in order to examine the mechanical response and failure mechanisms of textile composites under the on-axis mechanical loading. However, such textile laminates are often subjected to local off-axis tensile loading due to its wide application in plane and shell structures. [13]. Therefore, it is essential to experimentally assess deformation response and failure behavior in such loading cases, which will contribute to the safety and reliable design of composite structures.

Though the off-axis loading regime is uniaxial, multiaxial stress states will be generated due to the spatial variation of fiber orientation, leading to complex load-bearing mechanisms of textile composites from the interaction between the fibers and the matrix. The non-linear stress-strain response of textile composites is often observed in the global stress-strain curves under off-axis tensile loading [4,14–18]. The mechanical behavior has a strong sensitivity to the alignment of the fibers relative to the external loading. The angle between the fiber orientation and the loading direction significantly affects the degree of non-linear response [18,19]. Penava et al. [20] calculated the elastic constants of four woven fabrics for different fiber angles relative to the loading direction. The Young's modulus was assumed to be highest in the warp and weft direction, and the smallest at an angle of 45°. Work by Kawai et al. [16] compared the tensile mechanical properties of woven laminates with five different fiber orientations (0°, 15°, 30°, 45°, 90°) and demonstrated that with the increase of off-axis tensile angle, the off-axis elastic modulus and strength of the specimens reduce significantly and the stress-strain curve presents more significant non-linearity. It suggested that this phenomenon may be a result of the interaction of the tensile and shear stresses. A similar mechanical response was also found by Cai et al. [13,21] and

Koohbor et al. [4,15]. Godara et al. [17] employed the digital image correlation technique (DIC) method to experimentally investigate the effects of the fiber orientation on the mesoscale deformation and the multiple failure mechanisms of the woven textile composite. The composite exhibited a pronounced mechanical anisotropy at both macro and mesoscale. In addition, the full-field strain distribution at mesoscale and the microstructure of the material showed a strong correlation. Koohbor et al. [4] investigated the multi-scale deformation and failure mechanisms of an orthogonally woven composite at different off-axis angles. At meso scale, a high local strain gradient was found and the level of inhomogeneity was observed to be more obvious in the off-axis condition. In general, the failure of on-axis and off-axis textile composite indicates a noticeable brittle-natural feature [16,17], but especially for large off-axis angles such as 30° and 45°, the textile specimens are fractured after large elongation. The failure modes of specimens loaded in directions parallel to the 0° and 90° fiber orientations are often observed as fiber-pull out, and a rather flat fracture surface can be formed. In the case of off-axis specimen at 45° angle, the local shear strain in matrix-rich regions is the driving cause of failure, leading to a conical rough shear-type fracture surface [17]. In addition, the occurrence of fiber rotation in off-axis conditions has a predominant influence on the deformation response and loading-bearing mechanism of textile composites [15].

A more detailed literature survey indicates that more quantitative knowledge on the deformation response relative to the off-axis angle is still not fully established, in particular, the investigation of the relation between the deformation response and failure behavior of textile composites. Investigating the quantitative relation in the off-axis loading condition is essential to deeply understand the failure physics of textile composites. In view of this, this work presents a detailed analysis of the mesoscale deformation response and failure behavior of an orthotropic textile composite with different off-axis angles under tensile loading. Digital image correlation (DIC) was used to capture the full-field displacement and strain distributions at mesoscale. Based on the experimental data, a quantitative relation of deformation response is established. In addition, the effect of off-axis angles on fracture behaviors is also analyzed by mesoscopic and microscopic observation techniques.

2. Experiments

2.1. Material and specimen description

The material studied is a 1.6 mm thick, eight layer, plain woven composite made of carbon fiber (T300H) and thermosetting epoxy resin (E207). The two-dimensional plain woven fabric laminates consist of two mutually orthogonal fiber bundles (warp and weft) with 3K filaments per bundle. The warp and weft fiber bundles are interlaced to each other in an "one under- one over" pattern, forming unit cells of ~2.0×2.0 mm^2 dimensions. The volume fraction of carbon fibers is approximately 0.56, and the laminate density is about 1510 kg/m^3. The laminates were produced by using autoclave molding technique. In this technique, the prepregs were firstly stacked in the mold cavity, and then transferred to autoclave after degassing. A pressure of five bars was applied while the mold was heated to 80 ℃ for 20 min. The composite laminates were post-cured in the mold at 130 ℃ for two hours and taken out from the mold after cooling to 60 ℃. The symmetrical weaving architecture enables the mechanical properties to be the same in the warp and weft directions [13]. Therefore, in this work, only four off-axis angles (i.e. θ = 0°, 15°, 30° and 45°) were considered. Rectangular specimens of 220 mm long and 25 mm wide were cut from 670 mm by 440 mm laminate sheets using a waterjet machine to ensure good edge quality. Three specimens were tested for each off-axis angle 0°, 15°, 30° and 45°. To reduce the effects of steel grips, 2mm glass/epoxy composite tabs were bonded to the ends of the specimens with epoxy adhesive. A schematic view of the tensile specimens is illustrated in **Fig. 1**.

2.2. Test preparation

Tensile tests were carried out at room temperature using a 100 kN MTS servo-hydraulic machine (**Fig. 2 a**), following ASTM D3090 standard [22]. Loading was applied until fracture by displacement control at a rate of 1.44 mm/min, which was equivalent to the strain rate of 2×10^{-4} s^{-1}. Here, the two-dimensional digital image correlation (2D DIC) technique [23,24] was used to obtain the full-field displacement and strain data. To facilitate the DIC method, an airbrush was used to spray a random white speckle pattern on the black surface of each specimen. With this spraying method, a typical high contrast speckle pattern with the average speckle size of ≈30 um was achieved as shown in **Fig. 2 b**. During the loading, a single charge-coupled device (CCD) camera equipped with a 90mm lens was employed to capture the images from the specimen

surface; here, the images were taken at a rate of 2 HZ. The displacement and strain fields were analyzed using commercial software VIC-2D 2009 with subset and step sizes of 31 and 6 pixels, respectively. Details of the parameters used for the DIC procedure are shown in Table 1. In addition, scanning electron microscopy (SEM) was employed to observe the fracture morphologies of off-axis specimens.

3. Results and discussion

3.1. Stress–strain curves

Fig. 3 illustrates the tensile stress-strain curves of the tested specimens with different fiber orientations. The tensile stress (σ_x) was determined by dividing the applied load by the cross-sectional area, and the tensile strain was obtained by averaging the full-field axial strain component (ε_x) extracted from DIC at mesoscale. A remarkable nonlinear response from the off-axis specimens is clearly visible. As the loading progresses, a significant knee feature is observed in the curves of off-axis specimens (θ=15°, 30° and 45°), reflecting the reduction of material stiffness. Meanwhile, elastic modulus and tensile strength significantly drop with the fiber orientation change from 0° to 45° [16]. However, the knee-feature phenomenon does not occur in the on-axis (θ=0°) case. The on-axis stress-strain curve is monotonically linear and smooth up to failure.

To provide a quantitative assessment, the mechanical parameters of specimens with different fiber orientation angles were obtained by extracting the data from DIC and are listed in **Table 2**. Here, the linear regression fit was performed in the initial elastic region of stress-strain curves for each off-axis case to obtain the corresponding Young's modulus (E). Compared with the on-axis specimens, the elastic moduli (E) and failure strength (σ_f) values of specimens at θ=45° decrease by about 82.1% and 75.7%, respectively. With the increasing fiber orientation angle from 0° to 45°, the ductility of this material simultaneously increases, consequently the failure strain (ε_f) increases by about 12 times. It suggests that the mechanical properties of this material strongly depend on the reinforcing fiber orientation relative to the applied load.

In fiber-reinforced polymer composites, this anisotropic mechanical response can be explained by the load-bearing mechanisms of specimens with different off-axis angles. For the on-axis specimens (θ=0°), the stiffer reinforcing carbon fibers, which possess excellent tensile

strength and stiffness, take most of the applied load. In contrast, the softer polymer matrix has much lower strength compared with the carbon fibers. Once the fibers failed, almost all the applied load will be transferred to the soft matrix, which far exceeds the strength of the matrix, resulting in catastrophic failure. Therefore, the specimens with θ=0° exhibit high tensile strength and low ductility at fracture. However, due to the change of the off-axis orientation from 0° to 45° relative to the tensile load direction, the stiffer fibers, and the compliant matrix will share the applied tensile load [17]. Initially, most of the applied load is carried by the matrix, and shear flow occurs in the matrix material even at low external load. As the loading process progresses, the matrix starts dominating the mechanical behavior. Once the local shear stress in the matrix exceeds the shear strength, plastic flow occurs and the fiber bundles partially undergo stretching and realigning towards the loading direction (fiber trellising phenomenon [4,25]), consequently exhibiting the large non-linear deformation response at macroscopic scales.

3.2. Deformation response and failure strength

Under the off-axis loading, fiber trellising phenomenon leads to the large non-linear deformation response especially when the off-axis angle is large, e.g. θ=30°, 45°. To quantitatively analyze the stretching and rotation of fiber bundles, all relevant data were extracted from DIC measurements [15]. The stretch ratio of the fiber bundles is specified by, $\delta_\theta = \frac{\Delta l}{l_0} = \frac{l_i - l_0}{l_0}$, where the initial length l_0 and the deformed length l_i are defined as:

$$l_0 = \sqrt{(x_B - x_A)^2 + (y_B - y_A)^2} \tag{1}$$

$$\begin{aligned} l_i &= \sqrt{(x_{B'} - x_{A'})^2 + (y_{B'} - y_{A'})^2} \\ &= \sqrt{[(x_B + u_B) - (x_A + u_A)]^2 + [(y_B + v_B) - (y_A + v_A)]^2} \end{aligned} \tag{2}$$

respectively.

The rotation angle of the fiber bundles can be written as, $\Delta\theta = \theta_i - \theta_0$, where the initial angle θ_0 and the deformed angle θ_i are expressed as:

$$\theta_0 = \tan^{-1}\left(\frac{x_B - x_A}{y_B - y_A}\right) \tag{3}$$

$$\theta_i = \tan^{-1}\left(\frac{x_{B'} - x_{A'}}{y_{B'} - y_{A'}}\right) = \tan^{-1}\left[\frac{(x_B + u_B) - (x_A + u_A)}{(y_B + v_B) - (y_A + v_A)}\right] \tag{4}$$

respectively. Note that in the above equations (1), (2), (3) and (4), x_k and y_k indicate the initial coordinates at the measuring point k (k=A or B, here), u_k and v_k are the x-direction (axial) and y-direction (transverse) displacements, respectively.

The relationship between the stretch ratio (δ_θ) and the global axial strain (ε_x) for specimens with different off-axis angles is exhibited in **Fig. 4**. With the increase of the global strain, the stretch ratios of all specimens exhibit approximately monotonic linear response. The slope of specimens with θ=0° is close to 1% (The slop = The stretch ratio / The global strain), but the increase of the off-axis angles, the deviation between the stretch ratio and the strain obviously becomes larger, which is attributed to the load-bearing mechanism. For the case of θ=0°, the stiff fiber bundles take almost all the applied load during loading. Meanwhile, the crimped fiber bundles tend to straighten out with the increasing load. However, due to the internal architecture characteristics of the plain woven composite, the straightening magnitude is limited. As the off-axis angles increase, the matrix takes more load while the straightening trend of fiber bundles is becoming less pronounced. The softer matrix shows a more significant role in the load-bearing mechanism and induces a larger global strain, but does not have much effect on the elongation of fiber bundles. The above discussion may explain why the stretch ratios at failure are all about 1% for the four configurations while the strain levels are completely different.

Fig. 5 shows the variation of the rotation angle of fiber bundles with the increase of the global axial strain. It is clearly observed that in contrast with the relationship between stretch ratio and off-axis angle, the rotation angles of the off-axis specimens at failure strain remarkably increase with the increasing off-axis angle. This suggests that in fiber trellising phenomenon, compared with the stretching of fiber bundles, the rotation has a dominant influence on the mechanical behavior of this material. Owing to the important influence of off-axis angles on the mechanical properties (e.g. failure strength) of woven composite, it is worthwhile to investigate whether there is a certain relationship between the rotation of fiber bundles ($\Delta\theta$, i.e. fiber trellising) and the off-axis angles (θ) of the tested specimens.

The relationship between the off-axis angle (θ) and the rotation angle ($\Delta\theta$) at the instant of failure is shown in **Fig. 6 (a)**. The experimental data was processed by curve-fitting, and indicates that the rotation angle at failure was approximately a quadratic function of the off-axis angle. The

quantitative relationship can approximately be expressed as,

$$\Delta\theta=\begin{cases} k\cdot\theta^2 & 0°\le\theta\le 45° \\ k\cdot(90°-\theta)^2 & 45°<\theta\le 90° \end{cases} \quad (5)$$

Where the constant k=0.00293, the coefficient of determination R-square=0.9968, a value close to 1 indicates that the fit is a good one. In order to verify the validity of the above relationship, previous testing of rotation angles at different off-axis angles in the literature [15] were referenced and processed. As expected, although the plain woven composite used in the literature [15] is different from that of this present work, a similar quantitative relationship can be obtained, in comparison with Equation (5). For the quantitative relationship in the literature [15], the constant k=0.00413, the coefficient of determination R-square=0.9736, as shown in **Fig. 6 (b)**. Therefore, it suggested that this kind of quantitative relationship may be less affected by the material constituents, but more because of the plain woven architecture.

Material strength is one of the most important mechanical properties in most engineering applications. Based on the above analysis, the relationship between the failure strength and the rotation angle of fiber bundles is further investigated in this work. Tsai-Wu failure criterion [26,27] is applied to predict the off-axis strength. The criterion is a failure-mode-independent and stress-based criterion, which has been proven to be applicable to this case under tensile loading [28].

In the plane-stress condition, the failure criterion has the following form:

$$\frac{\sigma_1^2}{X_tX_c}+2F_{12}\sigma_1\sigma_2+\frac{\sigma_2^2}{Y_tY_c}+(\frac{1}{X_t}-\frac{1}{X_c})\sigma_1+(\frac{1}{Y_t}-\frac{1}{Y_c})\sigma_2+\frac{\tau_{12}^2}{S_{12}^2}=1 \quad (6)$$

Where X_t, X_c are the uniaxial tensile (index t) and compressive (index c) strengths in the longitudinal (X) direction respectively, Y_t and Y_c are the tensile and compressive strengths in the transverse (Y) direction, S_{12} is the shear strength, and F_{12} is the interaction coefficient of the normal stresses (σ_1 and σ_2). In this work, $F_{12}=-\frac{1}{2}\sqrt{\frac{1}{X_tX_cY_tY_c}}$.

For the off-axis specimen under uniaxial tensile loading (σ_x), the stress components can be expressed as functions of the orientation angle θ, and given as

$\sigma_1=\sigma_x\cos^2\theta,\ \sigma_2=\sigma_x\sin^2\theta,\ \tau_{12}=-\sigma_x\cos\theta\sin\theta$. Therefore, the criterion can be rewritten as

$$F_{xx}\sigma_x^{\,2} + F_x\sigma_x = 1 \tag{7}$$

Where the strength components F_{xx} and F_x are given as:

$$F_{xx} = \frac{\cos^4\theta}{X_t X_c} + \frac{\sin^4\theta}{Y_t Y_c} + (\frac{1}{S_{12}^2} + 2F_{12})\cos^2\theta\sin^2\theta \tag{8}$$

$$F_x = (\frac{1}{X_t} - \frac{1}{X_c})\cos^2\theta + (\frac{1}{Y_t} - \frac{1}{Y_c})\sin^2\theta \tag{9}$$

Due to the architecture symmetry of the plain woven composite studied in this work, this material has the same in-plane mechanical properties in the longitudinal (x) and transverse (y) directions. Therefore, the in-plane strength values obtained from basic mechanical tests are listed in Table , where the shear strength S_{12} was determined by tensile tests for 45° off-axis specimens.

The failure strengths of the tested specimens with different fiber orientations are shown in **Fig. 7**. The strengths are significantly dependent on the off-axis angles as described earlier. For the different off-axis cases, the predicted strengths have good agreement with the experimental data. It clearly suggests that this criterion has an excellent forecasting capability for the tensile strength of plain woven composite with different off-axis angles.

As discussed above, both the rotation angle and the failure strength are functions of the off-axis angles. In this case, the relationship between the rotation angle and the failure strength can be derived from Equations (5) and (7), and expressed as

$$\sigma_f^{\theta} = f(\Delta\theta) \tag{10}$$

Fig. 8 demonstrates the negative correlation between the failure strength and the rotation angle. The particular significance in the determination of quantitative relationship is that the obtained results will contribute to accurately predicting and modeling the structural and mechanical responses of the plain woven composite, optimizing the material design and ensuring reliable service.

3.3. Failure mechanism

Fig. 9 illustrates the front view of the fractured specimens with θ=0°, 15°, 30°, 45°. A nearly flat fracture edge almost perpendicular to the applied loading can be observed for the on-axis specimens (θ=0°) (**Fig. 9 a**), which is an indication of brittle fracture mode. For the cases of θ=15°, 30°, 45°, the final fracture approximately takes place along the orientation of fiber

bundles. The fracture surfaces of all the off-axis specimens have a brushy failure appearance. Note that the fracture surface at θ=15° contains both on-axis and off-axis fracture morphologies (**Fig. 9 b**). It suggests that for this case, the specimens are under a transitional condition from fiber-dominated to matrix-dominated failure.

The brushy fracture surface, which comprises separated fiber bundles, at lager off-axis angles (i.e. 30°, 45°) indicates that during the applied loading, the combination of in-plane fiber rotations and the shared loading mechanism between the fibers and the matrix creates the shear stress which causes the shear-type deformation at the fiber/matrix interface. Moreover, in this case, this deformation mainly occurs in the matrix, leading to the nucleation and coalescence of microcracks. Hence, shortly before fracture, a significant amount of delamination has been developed by the accumulated cracks, which induces this "brushy" fracture. As shown in **Fig. 9 e,** the matrix debris on the specimen surface can be clearly observed, which could be attributed to the extrusion effect from the interweaving fiber bundles. The superficial layer of the specimen is peeled off due to the occurrence of debonding between layers. Due to the shear stress, many local debond cracks are formed along the fiber/matrix interfaces within fiber bundles, as shown by the yellow arrows of **Fig. 9 e**. In addition, more damage (i.e. delamination and bundle cracks, **Fig. 9 f**) is found closer to the edges, which could be attributed to the free-edge effect [29].

Fig. 10 shows the fracture micromorphologies observed by SEM. In the on-axis case (**Fig. 10 a**), the deep pockets formed by fiber pull-out mechanism indicate the fiber/matrix interfacial debonding. During the loading, the longitudinal fibers are in an iso-strain condition. However, when some local longitudinal fibers have been broken, the softer matrix surrounding these fibers is incapable of bearing the large load transferred from the failed fibers. Therefore, the interfacial debonding and matrix cracks occur. At the ultimate failure, the instantaneous catastrophic failure results in the pull-out of the longitudinal fibers and breakage. On the other hand, the transverse fibers are in an iso-stress condition, contributing to the occurrence of smooth fracture surface (**Fig. 10 a**). It also implies that the applied loading is mainly carried by the longitudinal fibers. As depicted in **Fig. 10 b and d**, the fiber bundles of the off-axis specimen were pulled out by cluster, leading to the formation of deep pockets. Failure is expected to occur in the brushy fracture region, which supports the description earlier. Compared with the fractured sections of the fibers of on-axis specimens, there are numerous sites of oblique fracture sections of the fibers for off-axis

specimens [13] (**Fig. 10 d**), in some extent indicating the characteristics of off-axis failure mechanism at micro-scale.

As the above explanations for failure mechanism are just based on the phenomenology, full-field strain distributions of the investigated specimens obtained from DIC measurements are required. These observations are useful and important for analyzing ultimate strength and breaking mechanism. **Fig. 11** demonstrates the typical evolution of local vertical strain component (i.e. strain component in the *x*-direction) at selected global strain values of ε_x for the specimens with θ=0° and 30°, respectively. It is clearly observed that for the on- and off-axis specimens, the distributions of local strain are all inhomogeneity, and the level of inhomogeneity increases obviously with an increase of global strain. Also, in the case of off-axis specimens, the local vertical strain exhibits a more pronounced gradient, when compared to the on-axis specimens. High and low strain domains can be observed on the local strain maps regardless of on- and off-axis specimens, which is related to the load-bearing mechanisms discussed in section 3.1. For the on-axis specimens, similar to that found in the literature [15,30], the high vertical local strain is also identified within the regions containing mostly longitudinal fiber bundles. As described earlier, these fiber bundles parallel to the loading orientation carried most of the tensile load and thus underwent more local deformation as expected. However, in the off-axis cases, the high strain domains were developed within the epoxy-rich regions confined by the fiber bundles **(Fig. 11 b),** which could be explained by the off-axis load-bearing mechanism. As described in section 3.1, the compliant matrix initially took much of the tensile load, hence indicating higher deformation response, and the fiber bundles shared the remaining load. The strain maps show a periodic strain pattern at the middle stage of loading. However, as the loading increases, the periodicity of the strain pattern tends to be weakened at the advanced stage, e.g. ε_x=11.5%. Meanwhile, the grey parts of the DIC image at ε_x=11.5% **(Fig. 11 b)** indicate the regions of paint flaking, leading to the loss of data at these areas. As it can be seen, spotty strain concentrations appear, probably induced by local micro cracks developed within the matrix-rich regions. It suggests that these local cracks caused the imbalance of local load-bearing capacity.

With the increase of off-axis angles, a shear strain begins to develop in the matrix-rich regions between the longitudinal and transverse fiber bundles. **Fig. 12** illustrates the shear strain

fields obtained at two different global tensile strains (ε_x=5.75% and 11.5%). Significant shear strain stripes could be observed along the off-axis direction. Similar to what showed in the local vertical strain maps (**Fig. 11**), the level of shear-strain periodical-non-homogeneity increases with the increase of global strain. Prior to failure, the maximum value of local shear strain is about 74% of the global tensile strain. As discussed earlier, local microvoids in the matrix-rich areas weaken the local load-bearing capacity of the material. Under such high local shear strain, the material would eventually fail in a shear-type fracture, which is associated with a "brushy" shear fracture surface, as illustrated in **Fig. 10**.

4. Conclusion

The research work was focused on the tensile deformation response and failure behavior of an orthotropic textile carbon-epoxy composite with different off-axis angles. The global stress-strain responses, as well as the mechanical properties, were found to be strongly influenced by the off-axis angles, which was attributed to the load-bearing mechanism. Based on the mesoscale data extracted from DIC, the parameters in the fiber trellising (i.e. the stretch ratio and rotation angle of fiber bundles) were quantified, indicating that the rotation of fiber bundles rather than the stretch mainly affected the non-linear response. A quantitative relation between the rotation angle and the off-axis angle was established based on the analysis of experimental data. The predicted results from the established relation showed very good agreement with the experimental data at different off-axis angles. Furthermore, the Tsai-Wu strength criterion used for failure strength analysis exhibited high prediction precision. A negative correlation was observed according to the function curve between failure strength and rotation angle.

In addition, the fracture surface was nearly flat for the on-axis specimens, and brushy for the off-axis specimens. Due to the extrusion effect from interweaving fiber bundles, the matrix debris could be found on the specimen surface. A series of debond cracks along the orientation of fiber bundles was also observed. Deep pockets were found in SEM images of the on- and off-axis specimens. Oblique sections of fracture fibers were observed for off-axis specimens compared to those of on-axis specimens. Further investigation on failure mechanism was conducted through full-field strain analysis. The high vertical strain domains of the off-axis specimens were identified within the epoxy-rich regions while those of the on-axis specimens were developed within the

regions of fiber bundles, which led to different failure modes. For the off-axis case, a relatively high shear strain developed within the soft matrix regions, which eventually caused the shear-type fracture of this material. The periodicity of both vertical strain and shear strain became less obvious at the later stage of loading. It could be concluded that the local microcracks induced the reduction and imbalance of local load-bearing capacity.

Acknowledgments

This research did not receive any specific grant from funding agencies in the public, commercial, or not-for-profit sectors.

References

[1] Karahan M. Investigation of damage initiation and propagation in 2× 2 twill woven carbon/epoxy multi-layer composites. Text Res J 2011;81:412–28.

[2] Committee ACI. Guide for the design and construction of concrete reinforced with FRP bars, American Concrete Institute; 2001.

[3] Mouritz AP, Bannister MK, Falzon PJ, Leong KH. Review of applications for advanced three-dimensional fibre textile composites. Compos Part A Appl Sci Manuf 1999;30:1445–61.

[4] Koohbor B, Ravindran S, Kidane A. Meso-scale strain localization and failure response of an orthotropic woven glass-fiber reinforced composite. Compos Part B Eng 2015;78:308–18.

[5] De Carvalho N V., Pinho ST, Robinson P. An experimental study of failure initiation and propagation in 2D woven composites under compression. Compos Sci Technol 2011;71:1316–25.

[6] McLendon WR, Whitcomb JD. Characteristic progressive damage modes in a plain weave textile composite under multiaxial loads. J Compos Mater 2017;51:1539–56.

[7] Daggumati S, Van Paepegem W, Degrieck J, Xu J, Lomov SV, Verpoest I. Local damage in a 5-harness satin weave composite under static tension: Part II–Meso-FE modelling. Compos Sci Technol 2010;70:1934–41.

[8] Xu J, Lomov SV, Verpoest I, Daggumati S, Paepegem W Van, Degrieck J, et al. A progressive damage model of textile composites on meso-scale using finite element method: Static damage analysis. J Compos Mater 2014;48:3091–109.

[9] Dai S, Cunningham PR. Multi-scale damage modelling of 3D woven composites under uni-axial tension. Compos Struct 2016;142:298–312.

[10] Doitrand A, Fagiano C, Chiaruttini V, Leroy FH, Mavel A, Hirsekorn M. Experimental characterization and numerical modeling of damage at the mesoscopic scale of woven polymer matrix composites under quasi-static tensile loading. Compos Sci Technol 2015;119:1–11.

[11] Ivanov SG, Beyens D, Gorbatikh L, Lomov S V. Damage development in woven carbon fibre thermoplastic laminates with PPS and PEEK matrices: A comparative study. J Compos Mater 2017;51:637–47.

[12] Daggumati S, De Baere I, Van Paepegem W, Degrieck J, Xu J, Lomov SV, et al. Local damage in a 5-harness satin weave composite under static tension: Part I–Experimental analysis. Compos Sci

Technol 2010;70:1926–33.

[13] Cai D, Tang J, Zhou G, Wang X, Li C, Silberschmidt V V. Failure analysis of plain woven glass/epoxy laminates: Comparison of off-axis and biaxial tension loadings. Polym Test 2017;60:307–20.

[14] Ogihara S, Reifsnider KL. Characterization of nonlinear behavior in woven composite laminates. Appl Compos Mater 2002;9:249–63.

[15] Koohbor B, Ravindran S, Kidane A. Meso-scale study of non-linear tensile response and fiber trellising mechanisms in woven composites. J Reinf Plast Compos 2016;35:986–95.

[16] Kawai M, Taniguchi T. Off-axis fatigue behavior of plain weave carbon/epoxy fabric laminates at room and high temperatures and its mechanical modeling. Compos Part A Appl Sci Manuf 2006;37:243–56.

[17] Godara A, Raabe D. Influence of fiber orientation on global mechanical behavior and mesoscale strain localization in a short glass-fiber-reinforced epoxy polymer composite during tensile deformation investigated using digital image correlation. Compos Sci Technol 2007;67:2417–27.

[18] Pollock P, Yu L, Sutton MA, Guo S, Majumdar P, Gresil M. Full-field measurements for determining orthotropic elastic parameters of woven glass-epoxy composites using off-axis tensile specimens. Exp Tech 2014;38:61–71.

[19] Koohbor B, Mallon S, Kidane A, Sutton MA. A DIC-based study of in-plane mechanical response and fracture of orthotropic carbon fiber reinforced composite. Compos Part B Eng 2014;66:388–99.

[20] Penava Ž, Penava DŠ, Knezić Ž. Determination of the elastic constants of plain woven fabrics by a tensile test in various directions. Fibres Text East Eur 2014;104:57–63.

[21] Zhou G, Wang X, Li C, Deng J. Experimental investigation on mechanical properties of unidirectional and woven fabric glass/epoxy composites under off-axis tensile loading. Polym Test 2017;58:142–52.

[22] ASTM D3039/D3039M–17: Standard Test Method for Tensile Properties of Polymer Matrix Composite Materials. 2017.

[23] Pan B, Qian K, Xie H, Asundi A. Two-dimensional digital image correlation for in-plane displacement and strain measurement: a review. Meas Sci Technol 2009;20(6):062001.

[24] Hild F, Roux S. Digital image correlation: from displacement measurement to identification of elastic properties–a review. Strain 2006;42:69–80.

[25] Ullah H, Harland AR, Silberschmidt V V. Characterisation of mechanical behaviour and damage analysis of 2D woven composites under bending. Compos Part B Eng 2015;75:156–66.

[26] Liu K-S, Tsai SW. A progressive quadratic failure criterion for a laminate1. Compos Sci Technol 1998;58:1023–32.

[27] Tsai SW, Wu EM. A general theory of strength for anisotropic materials. J Compos Mater 1971;5:58–80.

[28] Soden PD, Hinton MJ, Kaddour AS. A comparison of the predictive capabilities of current failure theories for composite laminates. Compos Sci Technol 1998;58:1225–54.

[29] Mittelstedt C, Becker W. Free-Edge Effects in Composite Laminates. Appl Mech Rev 2007;60:217–45.

[30] Lomov S V, Ivanov DS, Verpoest I, Zako M, Kurashiki T, Nakai H, et al. Full-field strain measurements for validation of meso-FE analysis of textile composites. Compos Part A Appl Sci Manuf 2008;39:1218–31.

Table Captions

Table 1 Summary of the parameters used in DIC technique.

Table 2 The global mechanical properties of the tested specimens with different off-axis angles.

Table 3 Failure strengths of the plain woven composite.

Table 1 Summary of the parameters used in DIC technique.

Field of view dimensions (mm^2)	14 × 10.5
Subset size	31×31 Pixels square
Step size	6 pixels
Image rate	2 HZ
Pixel-to-length ratio	5.401 um/pixel
Lens (MLM-3XMP)	
Max. Magnification	0.3×-1.0×
Focus	90 mm
Camera (MER-500-7UM/UC)	
Pixel Array	2592 × 1944 pixels
Total Pixels	5 Megapixels

Table 2 The global mechanical properties of the tested specimens with different off-axis angles.

θ(°)	E (GPa)	ν	σ_f (MPa)	ε_f (%)
0	72.59	0.035	762.19	1.05
15	27.69	0.574	319.36	3.69
30	13.35	0.851	219.97	11.70
45	10.50	0.862	185.16	13.32

E: the global elastic modulus; ν: Poisson's ratio; σ_f: the failure strength; ε_f: the failure strain

Table 3 Failure strengths of the plain woven composite.

X_t [MPa]	X_c [MPa]	Y_t [MPa]	Y_c [MPa]	S_{12} [MPa]
762.19	721.42	762.19	721.42	92.58

Figure Captions

Figure 1 Schematic view of the tensile specimens (Unit: mm). The definition of coordinate system is also shown.

Figure 2 (a) The tensile experimental set-up used to capture the deformation response of tested specimen, with the typical speckle pattern on the specimen surface is shown in (b).

Figure 3 The axial tensile stress–strain curves of off-axis specimens.

Figure 4 Stretch ratio of fiber bundles versus axial strain for various fiber orientations.

Figure 5 Rotation angle of fiber bundles versus axial strain for various fiber orientations.

Figure 6 Variation of the rotation angle of fiber bundles ($\Delta\theta$) as a function of the off-axis angle (θ) in (a) this paper, and (b) the literature [15].

Figure 7 Tensile failure strength (σ_f) as a function of the off-axis angle (θ).

Figure 8 Variation of tensile failure strength (σ_f) as a function of the rotation angle ($\Delta\theta$).

Figure 9 Optical images of fractured specimens with (a) θ=0°, (b) θ=15°, (c) θ=30° and (d) θ=45°.

Figure 10 SEM micrographs of fractured specimens with (a)(c) θ=0°, (b)(d) θ=30° (Oblique sections of fibers was highlighted with yellow encircles).

Figure 11 Full-field distribution of local strain component ε_x for tested specimens at different values global tensile strain ε_x, (a) θ= 0° and (b) θ= 30°.

Figure 12 Full-field distribution of shear strain (ε_{xy}) for tested specimens with θ= 30° at (a) ε_x=5.75%, (b) ε_x=11.5%.

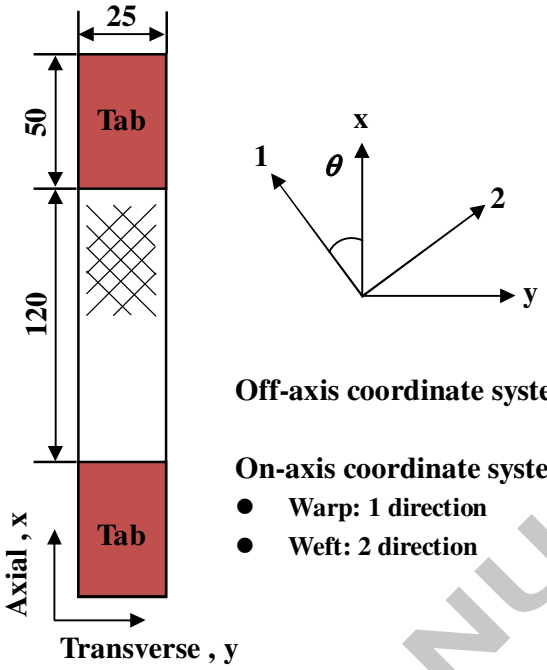

Figure 1 Schematic view of the tensile specimens (Unit: mm). The definition of coordinate system is also shown.

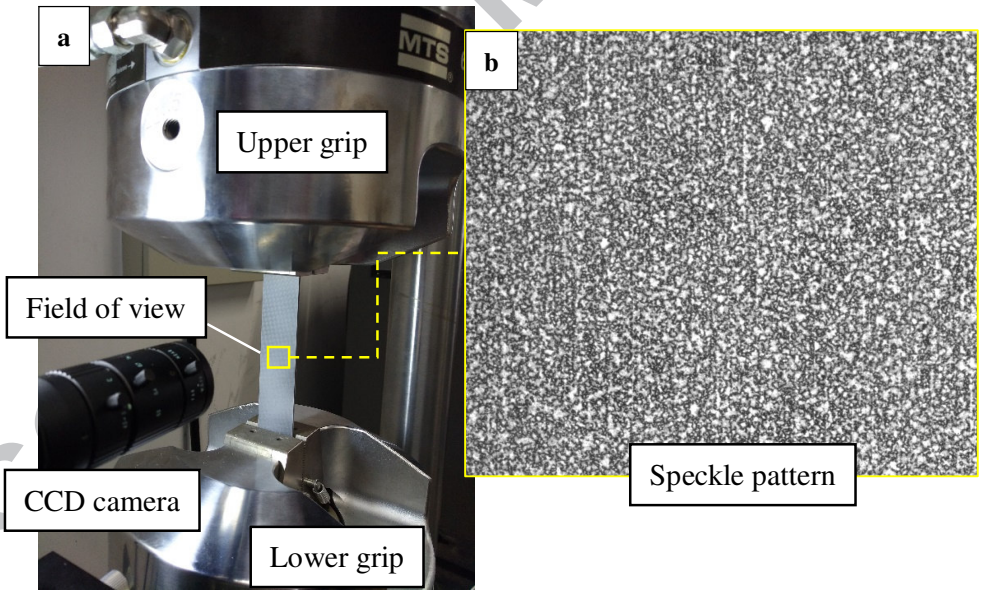

Figure 2 (a) The tensile experimental set-up used to capture the deformation response of tested specimen, with the typical speckle pattern on the specimen surface is shown in (b).

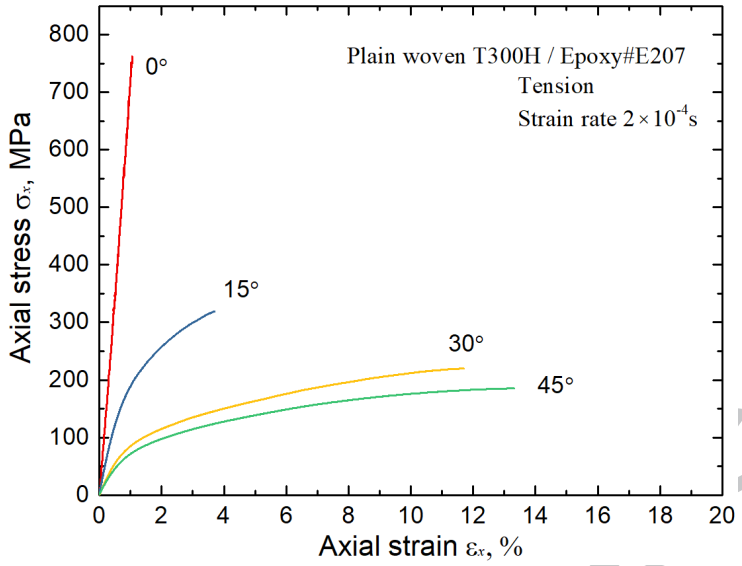

Figure 3 The axial tensile stress–strain curves of off-axis specimens.

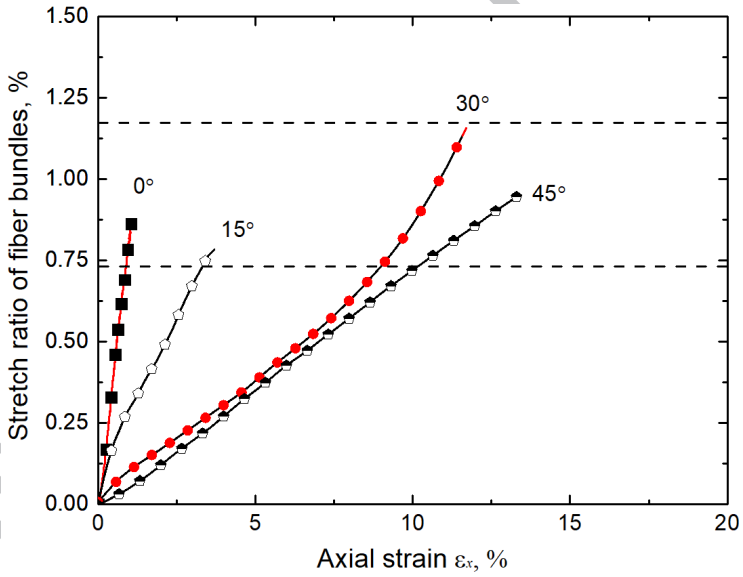

Figure 4 Stretch ratio of fiber bundles versus axial strain for various fiber orientations.

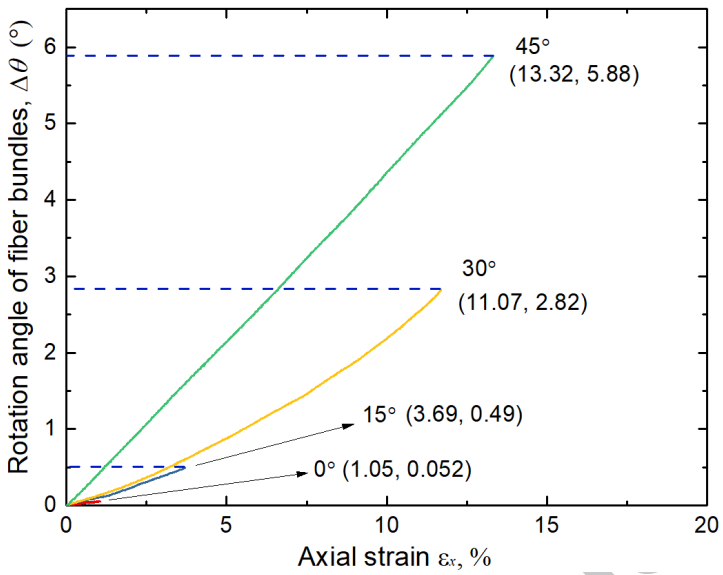

Figure 5 Rotation angle of fiber bundles versus axial strain for various fiber orientations.

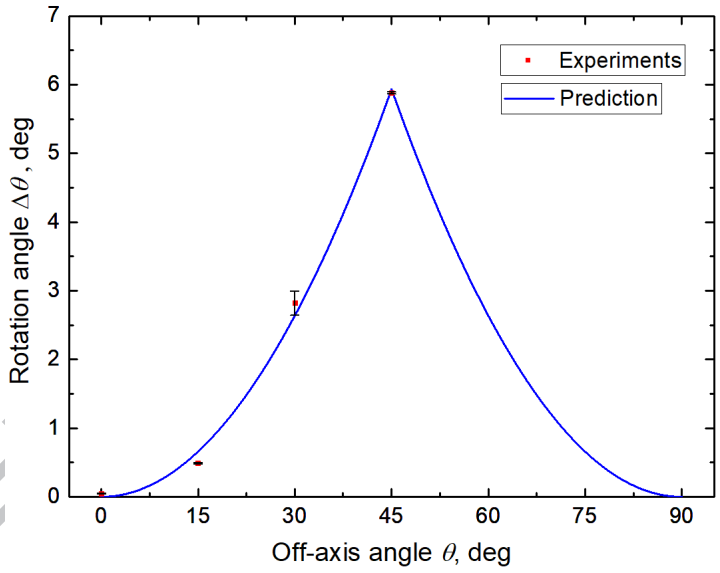

(a)

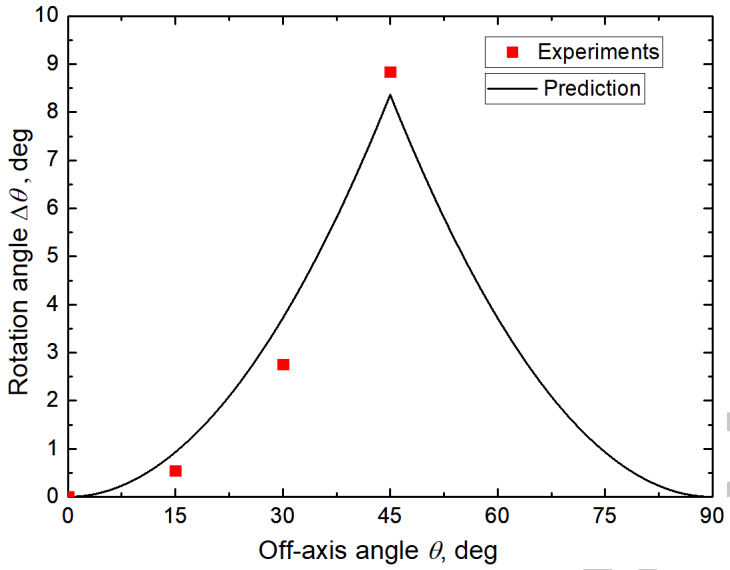

(b)

Figure 6 Variation of the rotation angle of fiber bundles ($\Delta\theta$) as a function of the off-axis angle (θ) in (a) this paper, and (b) the literature [15].

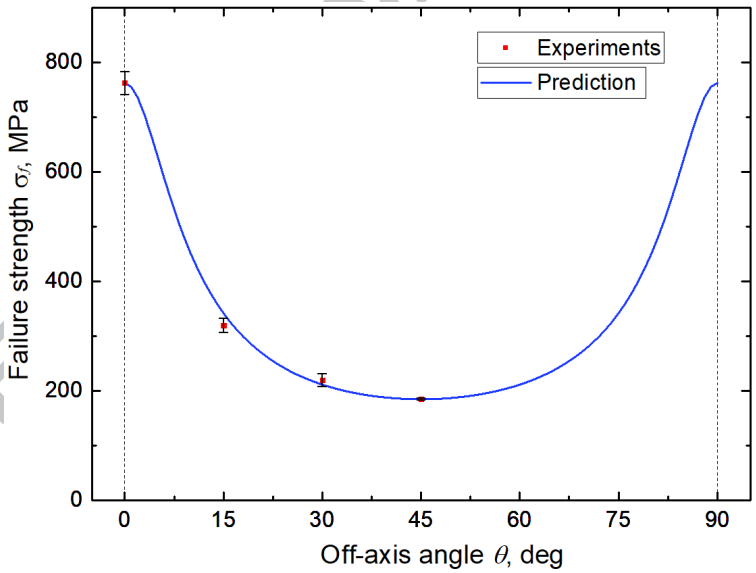

Figure 7 Tensile failure strength (σ_f) as a function of the off-axis angle (θ).

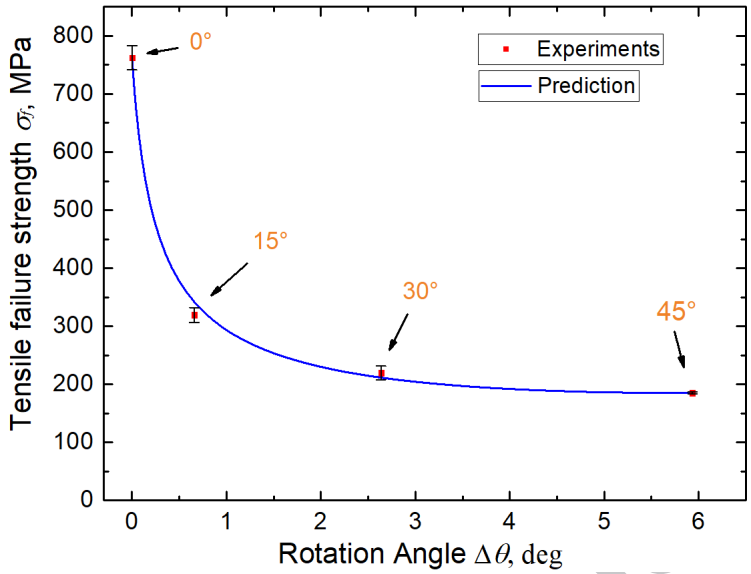

Figure 8 Variation of tensile failure strength (σ_f) as a function of the rotation angle ($\Delta\theta$).

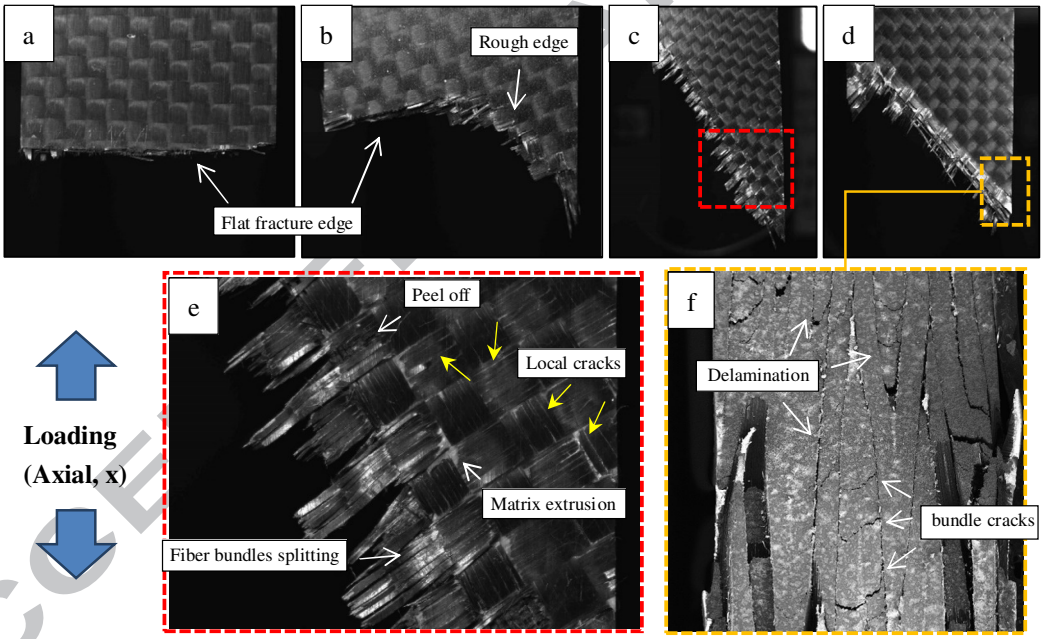

Figure 9 Optical images of fractured specimens with (a) θ=0°, (b) θ=15°, (c) θ=30° and (d) θ=45°.

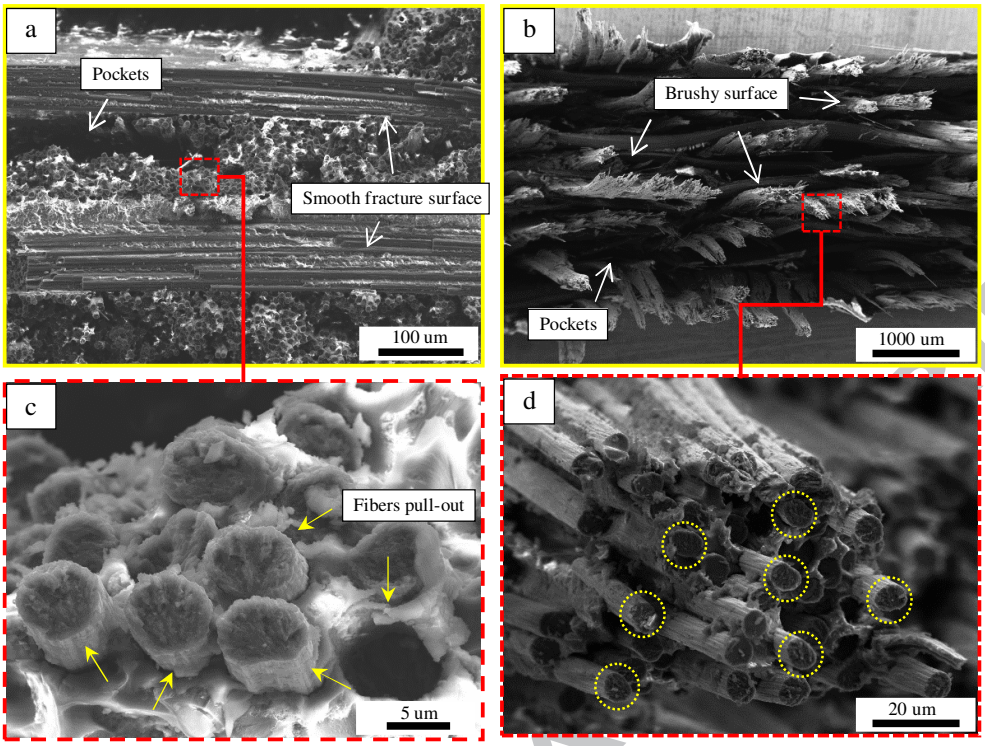

Figure 10 SEM micrographs of fractured specimens with (a)(c) θ=0°, (b)(d) θ=30° (Oblique sections of fibers was highlighted with yellow encircles).

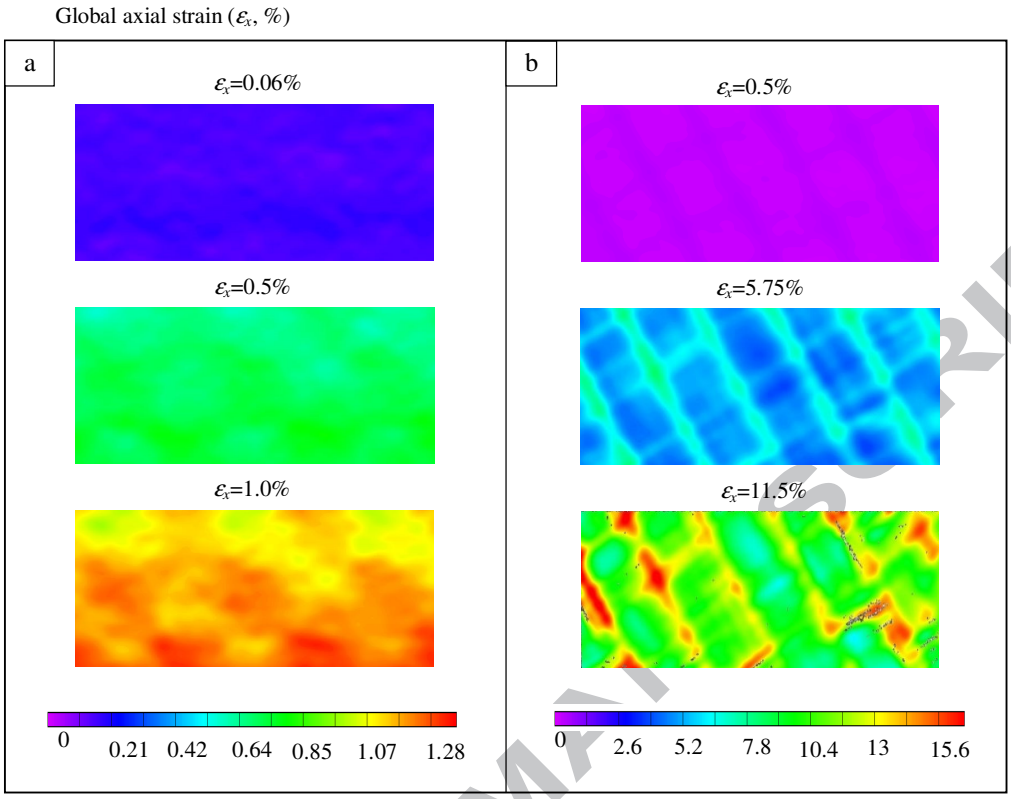

Figure 11 Full-field distribution of local strain component ε_x for tested specimens at different values global tensile strain ε_x, (a) θ= 0° and (b) θ= 30°.

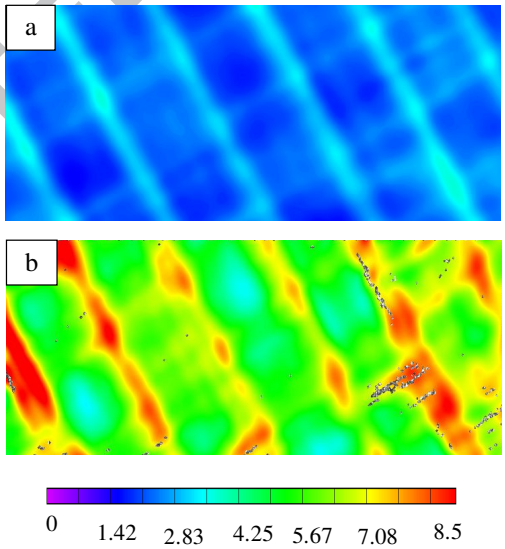

Figure 12 Full-field distribution of shear strain (ε_{xy}) for tested specimens with θ= 30° at (a) ε_x=5.75%, (b) ε_x=11.5%.